

Enhancing leaf area index and biomass estimation in maize with feature augmentation from unmanned aerial vehicle-based nadir and cross-circling oblique photography

Shuaipeng Fei^a, Shunfu Xiao^a, Qing Li^a, Meiyuan Shu^a, Weiguang Zhai^b, Yonggui Xiao^c, Zhen Chen^b, Helong Yu^d, Yuntao Ma^{a,*}

^a College of Land Science and Technology, China Agricultural University, Beijing 100193, China

^b Institute of Farmland Irrigation, Chinese Academy of Agricultural Sciences, Xinxiang 453002, China

^c National Wheat Improvement Centre, Institute of Crop Sciences, Chinese Academy of Agricultural Sciences, Beijing 100081, China

^d College of Information and Technology, Jilin Agricultural University, Changchun 130118, China



ARTICLE INFO

Keywords:
UAV photography
Plant phenotyping
Machine learning
Data augmentation
Multi-sensor

ABSTRACT

Rapid and accurate estimation of plant phenotypes plays a vital role in effective breeding and management of maize crops. Unmanned aerial vehicle (UAV) platforms are emerging as a valuable tool in the assessment of crop phenotypes, offering a promising avenue to enhance the accuracy and efficiency of phenotypic analysis. This study executed two UAV photography methods to acquire aerial images for the estimation of leaf area index (LAI) and above-ground biomass (AGB) in summer maize. Nadir photography was implemented to obtain data from three sources including multi-spectral (MS), RGB, and thermal infrared (TIR) sensors. Additionally, RGB imaging-based cross-circling oblique (CCO) photography was implemented to obtain accurate 3D point cloud data. The nadir photography data was processed to generate orthomosaic image and extract features including vegetation index, canopy cover, canopy height, canopy temperature, and textural information. Features including canopy occupation volume, plant area index, canopy cover, and canopy height were extracted from the CCO photography-derived point cloud data. Furthermore, a data augmentation method, called linear regression-based feature augmentation (LRFA), was proposed for augmenting features extracted from nadir and CCO photography. The results showed that the introduction of CCO photography improved the accuracy of LAI and AGB estimation during the big trumpet stage and LAI estimation during the milk stage compared to the integrated multi-source nadir photography data. Notably, the LRFA derived features outperformed raw features in the majority of modeling scenarios, with the random forest achieved an average accuracy (R^2) improvement of 6.1% for LAI estimation and 3.7% for AGB estimation. This study highlights the significance of combining different photography technologies and feature augmentation method for estimating maize phenotypes, providing novel opportunities for crop growth monitoring in modern agriculture.

1. Introduction

As one of the world's most important cereal crops, ensuring the effectiveness and excellence of maize production is of vital significance (Tester and Langridge, 2010). Traditionally, researchers have used phenotyping methods to study maize and develop ways to improve its performance. However, traditional manual methods have often been slow, laborious, and limited in scale, making it difficult to collect the vast amounts of data needed for large-scale studies (Che et al., 2020; Fei et al., 2023a; Xiao et al., 2022). In addition, relying solely on manual

measurements introduces subjectivity and increases the likelihood of errors, thereby compromising the accuracy and reliability of the data (Awika et al., 2019). The emergence of unmanned aerial vehicle (UAV) and advanced sensors has revolutionized crop phenotyping. By using UAV equipped with advanced sensors, data can be collected from large maize fields without the need for manual labor, saving time and reducing costs. The data collected from UAV platforms can be used to estimate crop traits such as canopy height (Wu et al., 2022), above-ground biomass (AGB) (Shu et al., 2022a; Yue et al., 2023), and grain yield (Fei et al., 2021; Shao et al., 2023), allowing for more accurate

* Corresponding author.

E-mail address: yuntao.ma@cau.edu.cn (Y. Ma).

analysis of maize growth and development.

Before the large-scale application of UAV technology for plant phenotyping, satellites, and ground-based spectroradiometers are the main remote sensing devices, and they have some drawbacks in collecting field data. The limited spatial and temporal resolution of satellites makes it difficult to capture detailed information of individual plants (Aasen et al., 2015; Floreano and Wood, 2015). Furthermore, satellite images are often affected by cloud cover and atmospheric interference, resulting in incomplete or unreliable data (Pan et al., 2021). On the other hand, ground-based spectroradiometers require researchers to physically move to different locations to collect data, which can be time-consuming and impractical for large-scale studies (Xie and Yang, 2020). UAV remote sensing has several advantages in plant phenotyping over satellite and ground remote sensing (Sidike et al., 2018; Xie and Yang, 2020). These include the ability to capture high-resolution imagery of individual plants, flexibility in data acquisition, the ability to capture data under specific conditions, cost-effectiveness, and time efficiency. Typical sensors affixed to UAVs for plant phenotyping encompass multispectral (MS), RGB, thermal infrared (TIR), hyperspectral, and LiDAR (Chen et al., 2022; Li et al., 2020; Maimaitijiang et al., 2020). These sensors facilitate the gathering of a broad spectrum of data concerning plant growth and developmental aspects. Among them, RGB sensor can capture color imagery of plants, allowing researchers to analyze plant morphology and identify changes in plant health over time (Chang et al., 2021; Garza et al., 2020). The MS sensor can detect different wavelengths of light, providing information on vegetation indices, growing condition, photosynthetic activity, and stress levels (Jiang et al., 2022; Pipatsitee et al., 2023; Wan et al., 2021). The TIR sensor can measure temperature variations, which can be used to monitor plant stress (Hou et al., 2021; Qin et al., 2022).

The combination of UAV sensors has been used to successfully evaluate various crop parameters. Multi-source data fusion can obtain higher accuracy in phenotype assessment than single sensor data since the spectral, structural, and thermal information of the canopy provides unique and complementary information that helps in the assessment of plant phenotypes (Maimaitijiang et al., 2020). Previous study demonstrated that predicting wheat yield by combining UAV RGB, MS, and TIR information can yield more accurate predictions than a single sensor (Fei et al., 2023b). The combination of these sensors has also been applied to estimate various parameters in other species, such as maize leaf area index (LAI) (Liu et al., 2021b), soybean phenotypes (Maimaitijiang et al., 2017), wheat nitrogen levels (Ding et al., 2022), and cotton yield (Feng et al., 2020). Fusion of hyperspectral data and other sensor data has also been reported to improve plant trait estimations such as potato biomass and wheat growth parameters (Li et al., 2020; Yue et al., 2018). In addition, LiDAR data were successfully combined with TIR and hyperspectral data for the sugar content assessment of sugar beets (Wang et al., 2022). For apple tree yield prediction, the combination of LiDAR and RGB, MS data also provided more accurate predictions (Chen et al., 2022). Significantly, the integration of structural data obtained through LiDAR with optical information can effectively address the saturation issue inherent in optical remote sensing (Chianucci et al., 2016; Wallace, 2013).

When choosing sensors for practical applications, the costs involved should be carefully considered. Hyperspectral and LiDAR sensors are generally more expensive than MS, RGB, and TIR sensors (Wang et al., 2022). Using low-cost MS sensors can help offset the lack of hyperspectral data to some extent. As an alternative to LiDAR, oblique photography, which is also capable of reconstructing the crop canopy structure from dense point clouds, has been successfully applied in crop plant height assessment (Che et al., 2020). Within this research, the approach of cross-circling oblique (CCO) photography was employed, involving the capture of multiple single-loop photographs from several meters above the canopy. This method was utilized to generate 3D models of the canopy and extract its structural attributes, which has shown good accuracy in calculation of organ-scale traits (Xiao et al.,

2023) but has not yet been applied to population trait analysis.

Previous research on the fusion of multi-source data has mostly involved directly using features extracted from different sensors as inputs to regression algorithms (Fei et al., 2023b; Maimaitijiang et al., 2020). Although this approach yielded promising outcomes, it may not represent the most efficient means of fully harnessing the information potential offered by multiple sensors. To comprehensively tap into the predictive capabilities of multi-source data, a feature augmentation method based on linear regression was introduced. This approach has the capacity to generate a substantial number of additional features that encompass information from diverse sensors. Based on the above, the overall goal of this study is to evaluate the combination of UAV nadir (MS, RGB, and TIR) and CCO (RGB) photography to monitor plant phenotypes under field conditions. The specific objectives are as follows: (a) To estimate maize LAI and AGB by combining spectral, temperature, and precise 3D structural information extracted from nadir and CCO photography using machine learning algorithm. (b) To compare the modeling accuracy of the proposed feature augmentation method with that of the conventional method.

2. Material and methods

2.1. Experimental design

During the summer maize growing season of 2022, an experiment was conducted in Xinxiang City, Henan Province, China, with precise geographic coordinates of $113^{\circ}45'42''E$ and $35^{\circ}08'05''N$. On June 15, 2022, ten varieties (Table S1) of maize were planted and subjected to four different fertilizer treatments: N0 (no fertilizer application), N1 ($80 \text{ kg}/\text{hm}^2$), N2 ($120 \text{ kg}/\text{hm}^2$), and N3 ($160 \text{ kg}/\text{hm}^2$). Each maize variety was replicated three times in each treatment, resulting in a total of 120 plots, each measuring 8 m^2 (2 m by 4 m). The field was optimally managed and strictly compliant with the prevailing environmental and climatic conditions throughout the study.

2.2. Field data collection

Phenotypic assessments in the field were executed during two critical growth stages: the big trumpet stage (or the 11-leaf stage) and the milk stage. Quantification of LAI was undertaken utilizing the SunScan canopy analyzer, a comprehensive system by Delta-T Devices Ltd., Cambridge, UK, comprising a probe (SS1), a sensor (BF5), and a handheld terminal (RPDA2), which was furnished with Sundata software. The LAI measurements were taken from diverse directions at the base of each plot, and an average was computed to derive a representative LAI value. In order to ensure congruence of data, LAI measurements were obtained before the acquisition of UAV images. A visualization of LAI distribution across all plots is presented in Fig. 4. To ascertain AGB, two uniform maize plants were meticulously selected from each plot and subjected to drying at 85°C in a dryer until their mass reached a consistent state. The AGB per unit area of maize was subsequently determined through the dry weight of the samples coupled with the population density. The distribution pattern of AGB is visually depicted in Fig. 4. The measurement of canopy height within each plot entailed the random selection of five plants, followed by the determination of the vertical distance from the ground to the tallest point on each plant using a ruler. The average height across these five plants was adopted as the representative canopy height for the respective plot. The distribution of canopy height is graphically represented in Fig. 4.

2.3. UAV nadir photography and image processing

UAV was harnessed in the investigations to carry out nadir photography employing three distinct sensors: MS, RGB, and TIR. Image acquisition was orchestrated through the utilization of two drones: an M210 drone (SZ DJI Technology Co., Shenzhen, China) outfitted with a

Red-Edge MX camera (MicaSense Inc., Seattle, USA) and a Zenmuse XT2 camera (SZ DJI Technology Co., Shenzhen, China) (Fig. 1) to facilitate MS and TIR imaging, along with a Phantom 4 RTK drone (SZ DJI Technology Co., Shenzhen, China) for RGB imaging. Notably, the Phantom 4 RTK drone incorporates DJI On-board D-RTK technology (Fig. 1D), enabling meticulous positioning data with an impressive precision of up to a centimeter. This technology supplies raw satellite observations and exposure event records, essential for post-processing kinematic differential corrections.

The Red-Edge MX camera encompasses five spectral lenses spanning blue (475 nm), green (560 nm), red (668 nm), red-edge (717 nm), and near-infrared (842 nm) wavelengths. It features a sunlight sensor that dynamically adjusts to mitigate inconsistencies in MS images (Hassan et al., 2019b). Within the camera, a monochrome sensor captures images at a resolution of 1280×960 pixels, with distinct bandwidths for various bands: red and red-edge boast a 10 nm bandwidth, blue and green possess a 20 nm bandwidth, and infrared maintains a 40 nm bandwidth. Rigorous radiometric calibration was undertaken both prior to and after each flight using a calibration board, effectuating the conversion of digital number values in the MS data to reflectance values. The Zenmuse XT2 camera, on the other hand, records thermal observations within the 7.5–13.5 μm spectral range. With a thermal sensitivity of 5 °C and an imaging resolution of 640×512 pixels. Meanwhile, the RGB camera that comes with the Phantom 4 RTK drone has a 20-megapixel ($5,472 \times 3,648$) resolution. DJI Pilot software was deployed for flight route planning. The UAV flights were meticulously executed under clear sky conditions, scheduled between 11:00 and 13:00 on the day of the field measurements, and maintained at a consistent altitude of 30 m to capture high-quality images. Notably, both the TIR and RGB imagery encompassed an 85 % front and side overlap. The MS camera,

due to variations in its field of view, exhibited a front overlap of 85 % and a side overlap of 90 %. Furthermore, to amplify the precision of image processing, 15 ground control points were evenly dispersed across the experimental area. These points were meticulously surveyed using a differential global navigation satellite system, serving to refine the accuracy of the overall process.

We utilized the Pix4Dmapper software (Pix4D SA, Lausanne, Switzerland) to carry out the orthorectification and mosaicking of the UAV-captured RGB, MS and TIR images. The key stages of this process encompassed image geolocation, the incorporation of ground control points, image alignment, the creation of dense point cloud data, digital surface model (DSM), orthomosaics, and performing radiometric calibration (Han et al., 2019).

2.4. UAV CCO photography

The methodology of CCO photography involves capturing multiple single-circle photographs (Fig. 2), with a distinction made between intra-circle and inter-circle overlap (Xiao et al., 2023), has not yet been used in AGB and LAI estimation. Intra-circle overlap pertains to the coverage between images within a single-circle photograph and is dictated by factors like flight height, circle radius, and camera field of view. On the other hand, inter-circle overlap refers to the coverage between two consecutive single-circle photographs and is determined by their overlap. Fig. 2B provides a visual of the CCO photography containing four single circles, featuring a 50 % inter-circle overlap. The green section indicates the region amenable to reconstruction, while the purple area represents the inscribed square within the reconstruction region. Reconstruction necessitates a minimum inter-circle overlap of around 50 %, which is achieved when the inscribed squares of adjacent



Fig. 1. UAV platforms and sensors.

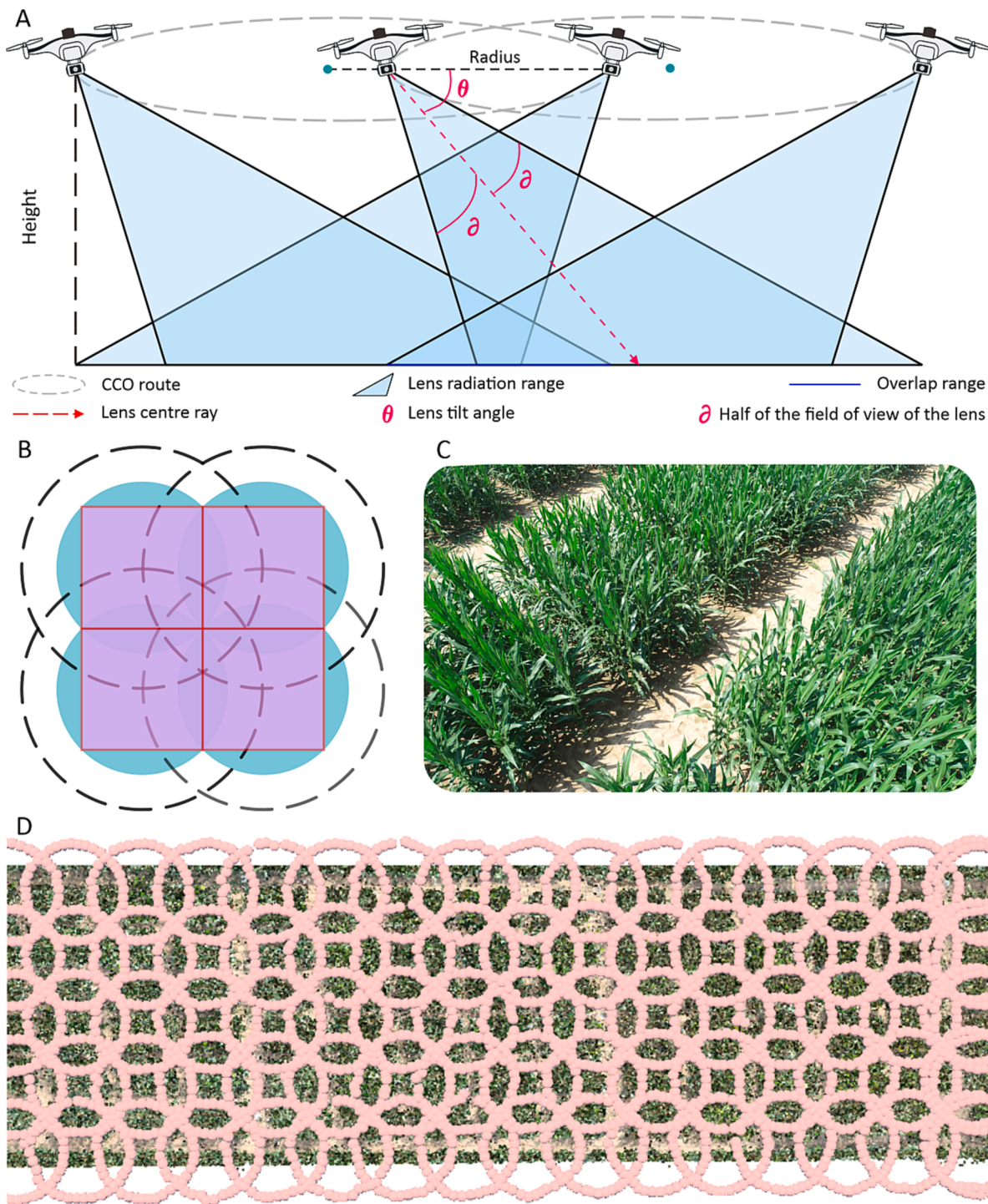


Fig. 2. (A) Side view of a CCO route consisting of two single circles with a 50% inter-circle overlap. (B) Top view of a CCO route consisting of four single circles with a 50% inter-circle overlap. (C) Image taken by CCO photography. (D) The actual flight path of the CCO route.

circular photographs are in contact.

The CCO photography was conducted simultaneously using two DJI Phantom 4 RTK drones. For the flights, the altitude was set at 4 m above the canopy (adjusted based on the canopy's height), the circle radius was set to 4 m, and the camera was positioned at a 45° angle. To ensure comprehensive image acquisition, the narrow and curved maize leaves required approximately 90 % intra-circle overlap and 60 % inter-circle overlap. Flight speeds were maintained at 0.2 m/s, with images taken at 2-second intervals while the camera was focused on the circle's center.

2.5. Reconstruction of 3D canopy structure from CCO photography images

The sequences of UAV images underwent processing utilizing Agisoft Metashape Professional Edition v1.7.3. This software employs a conventional structure-from-motion and multi-view stereo (SfM-MVS) workflow to detect distinctive key points and descriptors within the Pixel coordinate system (CS). Notably, Metashape was able to establish consistent descriptors for key points across varying lighting conditions during image capture, ensuring stability under different perspectives

and illumination. Subsequently, the software deduced camera parameters and positions by utilizing the identified key points and descriptors. This was followed by generating a sparse point cloud within the Camera CS. The transformation of the sparse point cloud into the Internal CS was achieved by employing internal and external camera orientation parameters. For enhancing point densities, the software executed dense point cloud reconstruction through MVS methods. The outcome, a dense point cloud, was exported within the UTM zone 49 N CS and subjected to denoising through the statistical outlier removal filter algorithm. Fig. 3 visually represents the distribution and height of 3D canopy of CCO-derived maize at the big trumpet stage. In order to systematically segment individual plots, a uniform division was applied based on their spatial arrangement within the experimental design. Each plot was then assigned a distinctive identifier based on its geographic location. This segmentation procedure encompassed two primary steps. Firstly, the manual identification of the four corners of each plot facilitated the establishment of spatial polygons, accomplished using the “SF” and “Raster” package in R v4.2.2. Subsequently, the dense point cloud underwent sequential segmentation by employing the Whitebox Tools library in Python, version 3.5.

2.6. Features extracted from nadir photography-based images

Various types of features were extracted from the nadir photography-based images. These features including band reflectance and DN values, vegetation indices, temperature information, texture features, and structural features (Fig. 4), which are listed in Table S2. The number of features of MS, RGB, and TIR are 38, 37, and 9, respectively.

2.6.1. Background removal and canopy cover extraction

The excess green minus excess red index (EXGR), derived from RGB band data, played a pivotal role in mitigating background noise and extracting canopy cover (CC). To pinpoint maize pixels within the UAV images, an initial binary mask was created using the EXGR values. Subsequently, this mask was utilized to partition the image into distinct segments: maize vegetation and background elements encompassing soil, shadows, and other ground features. Ultimately, the maize pixels

identified within each plot were divided by the total pixel count of that plot, culminating in the calculation of the CC. Importantly, the masks generated through the EXGR method also proved effective in eliminating background interference from MS and TIR images.

2.6.2. Vegetation indices and canopy texture information

The raw bands from MS and RGB orthomosaics were used as features to assess LAI and AGB. Furthermore, a selection was made from a variety of MS and RGB vegetation indices, previously employed for plant trait analysis. The pertinent equations for their computation, along with their respective sources, have been succinctly consolidated within Table S2. From the red-edge and NIR bands within the MS image, as well as each band within the RGB and TIR image, texture attributes were extracted. To accomplish this, the “GLCMTextures” package in R v4.2.2 was leveraged to compute texture characteristics rooted in gray level co-occurrence matrices (GLCM) (Haralick et al., 1973).

2.6.3. Canopy height

The DSM generated from digital images provides elevation information for plants, soil, and other ground objects (Bendig et al., 2015). To obtain the canopy height model (CHM), the DSM was subtracted from a digital terrain model (DTM) on a pixel-by-pixel basis. However, settling of the topsoil due to rainfall, irrigation, and other factors can cause a decrease in the true elevation value of the surface (Shu et al., 2022b). To overcome this, a contemporaneous DTM was generated in Pix4Dmapper using images that were captured at the same time as the DSM. The process involved filtering and classifying terrain points in a point cloud, based on their elevation, slope, and curvature, and then interpolating these points to generate an elevation grid that represents the terrain surface.

The intricate configuration of maize canopies introduces complexities, and the conventional method of computing canopy height by averaging pixel values across various leaves of multiple plants can lead to notable underestimations (Han et al., 2018). To circumvent this, the approach employed in this study involved the computation of canopy height through pixels captured from the upper leaves of multiple plants. Specifically, the 99 % quantile of pixel values within each plot, as

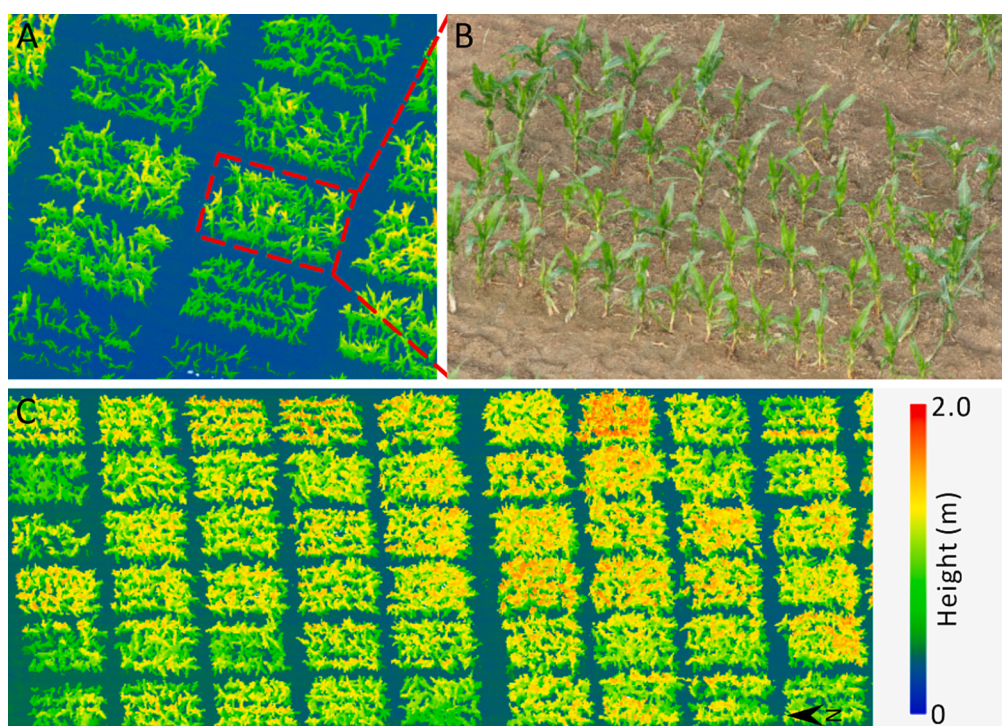


Fig. 3. 3D point cloud data (A and B) and canopy height (C) generated by image sequence from cross-circling oblique photography.

depicted by the CHM, was utilized to accurately signify the canopy height.

2.6.4. Canopy temperature information

The normalized relative canopy temperature (NRCT) was computed using UAV TIR imagery (Fig. 4). The formula is as follows:

$$\text{NRCT} = \frac{T_i - T_{\min}}{T_{\max} - T_{\min}} \quad (1)$$

where T_i represents the canopy temperature of the i th pixel, T_{\min} is the lowest temperature across the field trial, and T_{\max} is the highest temperature across the field trial.

2.7. Features extracted from reconstructed 3D canopy structure

Canopy architectural traits were extracted from the 3D structure, including canopy occupation volume (COV), plant area index (PAI), CC, and canopy height. To calculate COV, the canopy model was voxelized, with each voxel having a thickness of 1 cm, and the occupied voxels were determined by those containing triangles from the canopy model. The COV was obtained by calculating the total volume of these occupied voxels. PAI was obtained by dividing the total plant area by the canopy occupation area, which was calculated from the meshed canopy using Heron's formula. CC was calculated by dividing the occupied area by the total area of the horizontal plane. The canopy height was defined as the distance between the base point of the stem and the 99th percentile height. Additional details regarding the COV formulation can be found in Liu et al. (2021a), while information on Heron's formula can be found in Kendig (2000).

2.8. Development of a feature augmentation technology

To fully integrate the features extracted from different sources, a linear regression-based feature augmentation (LRFA) method was proposed in this study (Fig. 5). The steps of LRFA are as follows, using an example of combining all four sources of features (90 features in total):

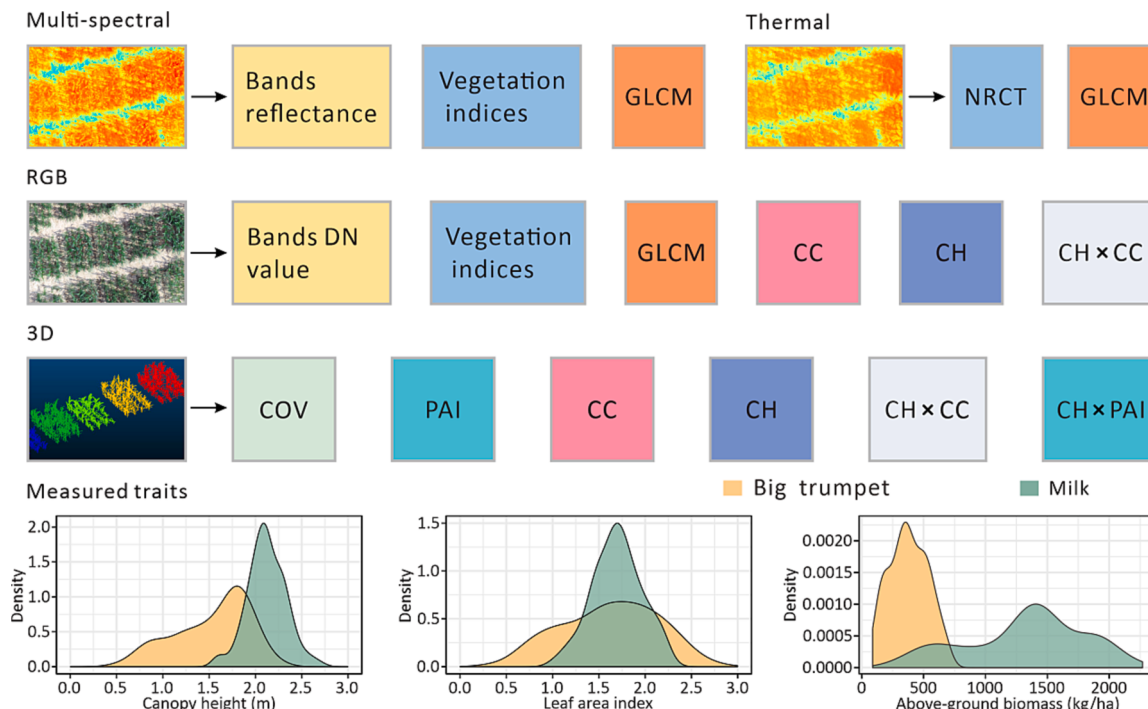


Fig. 4. The extracted features and the distribution of the measured phenotypes. GLCM gray level co-occurrence matrix, NRCT normalized relative canopy temperature, CC canopy cover, CH canopy height, COV canopy occupation volume, PAI plant area index.

- Initially, the dataset was partitioned into a training set and a test set using a predetermined ratio.
- On the training set, i features were randomly selected from the feature sets of MS, RGB, TIR, and 3D separately, resulting in a total of $4i$ features. The same features were also selected on the test set.
- These $4i$ features on training set were combined with the plant trait values and denoted as D . The 10-fold cross-validation was then performed on D using multiple linear regression (MLR). The out-of-sample prediction generated during the cross-validation process was used as a new training feature. The MLR model was trained using all the data of D and tested on $4i$ features on the test set. The output prediction was used as a new test feature.
- Step c) was repeated for n times to generate n new features in both the training and test datasets. Since the $4i$ features selected in each iteration were different, the features generated between different iterations were independent of each other. These n new features were combined with all the original features in the training and testing datasets, forming a new training set and a new test set with a dimension of $n + 90$.
- Training a machine learning model using the new training set created in step d), and evaluating its accuracy on the new test set.

The proposed LRFA (Fig. 5) method borrows a part of stacking regression, an ensemble learning method. In stacking regression, the out-of-sample prediction matrix generated by the level-1 of each base learner is used as the input features for the level-2, which improves the final model prediction. Every sampling performed in LRFA is equivalent to adding a new learner in stacking regression, and in turn the out-of-sample predictions obtained through MLR training can be used as new features. A detailed steps of the generation of new features using out-of-sample predictions is shown in Fig. S1. Considering the number of features for each sensor, this study sets i to 5 and n to 200 to verify the data fusion effect of LRFA. Additionally, we compared the performance of LRFA with the conventional data fusion method where the different types of features are combined and used as direct inputs for machine learning model training. It's worth mentioning that certain identical

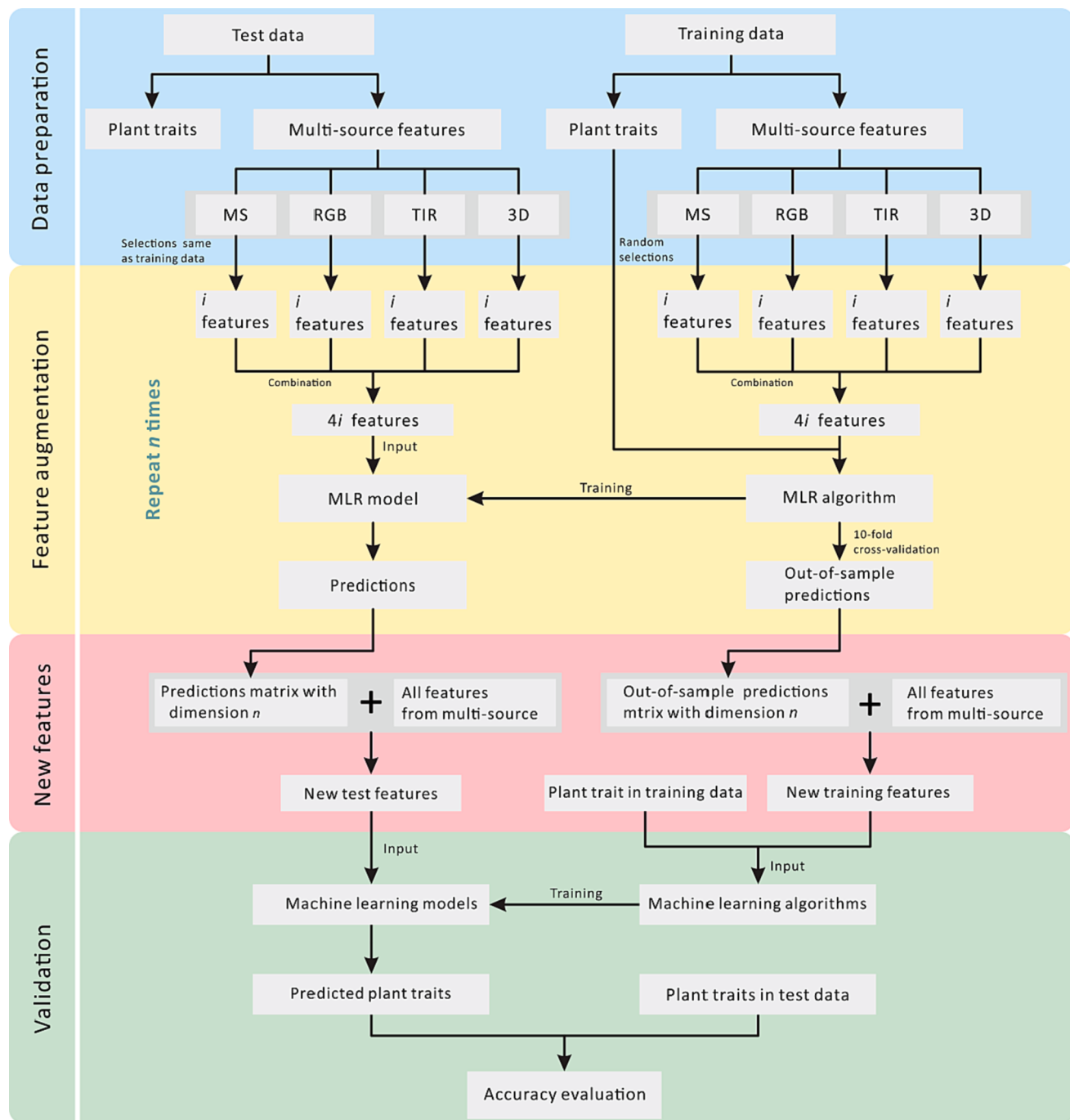


Fig. 5. The schematic of proposed linear regression-based feature augmentation method. MLR, multiple linear regression, MS multi-spectral, TIR thermal Infrared.

structural attributes (CC, CH, and CC × CH) were derived from both RGB and 3D data. To prevent redundant data, when incorporating both RGB and 3D features in the data combination, only the structural attributes within the 3D data are employed.

2.9. Modeling method and accuracy evaluation

The random forest algorithm (Breiman, 2001) was employed to construct regression models in this research. To gauge the predictive precision of the regression models, the outer cross-validation was adopted (Montesinos-López et al., 2019). This encompassed partitioning the accessible data into 5 equivalent folds, employing 4 of these folds for model training, and reserving the fifth fold for performance evaluation. This sequence was reiterated 5 times, with each fold assuming the role of

the validation set once. The ultimate model performance was computed as the mean across all 5 folds. Within each outer cross-validation training set, the inner 5-fold cross-validation was employed to determine the optimal hyperparameters (Montesinos-López et al., 2019). The outcomes of each fold were averaged to approximate the model's performance using a specific set of hyperparameters. Subsequently, the optimal hyperparameters were employed in the training set for outer cross-validation to train the model. The hyperparameters for random forest model were ascertained automatically through the "train" function in the "caret" package (R v4.2.2). The prediction performance was quantified using coefficient of determination (R^2) and root mean square error (RMSE):

$$R^2 = 1 - \frac{\sum_{i=1}^n (\hat{y}_i - y_i)^2}{\sum_{i=1}^n (y_i - \bar{y})^2} \quad (2)$$

$$\text{RMSE} = \sqrt{\frac{\sum_{i=1}^n (\hat{y}_i - y_i)^2}{n}} \quad (3)$$

where y_i and \hat{y}_i are the measured and the predicted phenotype value, respectively. \bar{y} is the mean of measured phenotype value and n is the total number of samples.

3. Results

3.1. Canopy height estimation

The correlations between UAV-extracted canopy height and measured canopy height are depicted in Fig. 6. The findings reveal that during both the big trumpet and milk stages, the canopy height calculated from the 3D model exhibited a stronger correlation with the measured canopy height compared to the CHM. Specifically, the R^2 between CHM-derived canopy height and measured canopy height stood at 0.78 (RMSE = 0.22 m) during the big trumpet stage, and 0.52 (RMSE = 0.17 m) during the milk stage. Meanwhile, the R^2 values between 3D model-derived canopy height and measured canopy height were 0.92 (RMSE = 0.13 m) and 0.71 (RMSE = 0.11 m) during the big trumpet and milk stages, respectively. The enhanced precision of the 3D model-derived canopy height can be attributed to the comprehensive depiction of plant shape and volume facilitated by COO photography, in contrast to the limitations of nadir photography.

3.2. Modeling and validation of LAI and AGB

3.2.1. Model performance for estimating LAI

In the context of the big trumpet stage, the results show that MS features achieved a superior accuracy in LAI estimation (Table 1), with an R^2 of 0.726 and an RMSE of 0.276. Notably, the R^2 value was higher for 3D features compared to both RGB and TIR features. In the majority of cases, combining data from multiple sources led to significant enhancements in LAI estimation compared to using single-source data. Specifically, the combination (LRFA) of MS, RGB, and 3D data outperformed all others, yielding an impressive R^2 of 0.791 and an RMSE of 0.235, which significantly surpassed the performance of the best single-source data (MS). During the milk stage, MS features continued to demonstrate superior performance, boasting an R^2 value of 0.537 (RMSE = 0.180). The 3D features exhibited a lower accuracy than RGB but still outperformed TIR. It's important to note that all combinations of multi-source data consistently yielded higher accuracy compared to using single-source data. The combination of MS, RGB and 3D features yielded the best estimation accuracy, with an R^2 of 0.654 and an RMSE of 0.154.

3.2.2. Model performance for estimating AGB

In big trumpet stage (Table 1), features from the MS sensor provide the most accurate estimation of AGB ($R^2 = 0.625$, RMSE = 94.4 kg/ha), followed by RGB ($R^2 = 0.622$, RMSE = 95.2 kg/ha), TIR ($R^2 = 0.618$, RMSE = 97.3 kg/ha), and 3D features ($R^2 = 0.570$, RMSE = 101.3 kg/ha). As expected, the combination of multi-source data yielded higher accuracy in AGB estimation. Combining the features (LRFA) from RGB, TIR, and 3D produced the highest prediction accuracy ($R^2 = 0.679$, RMSE = 87.5 kg/ha). In the milk stage, MS and RGB features

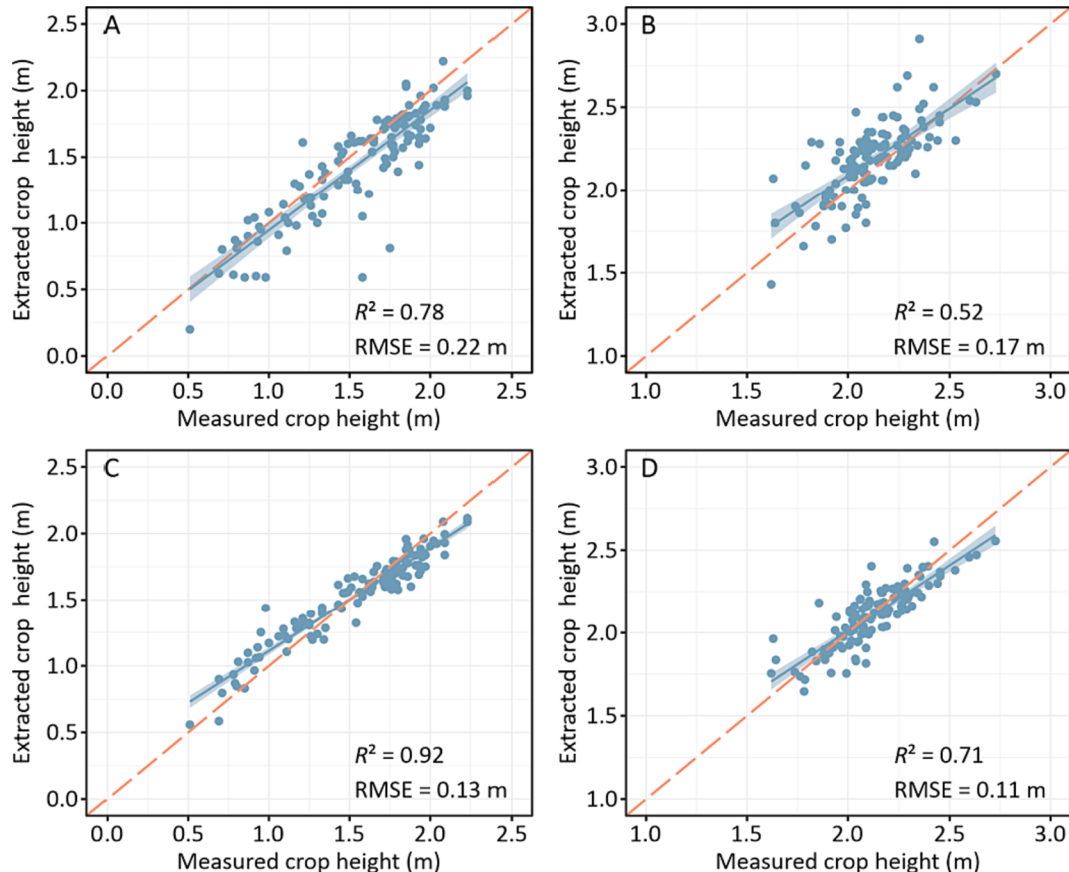


Fig. 6. Relationship between canopy height extracted by UAV and measured canopy height. A and B show the canopy height extracted by canopy height model at the big trumpet and milk stages, respectively. C and D show the canopy height extracted by 3D model at the big trumpet and milk stages, respectively.

Table 1

Accuracy parameters for leaf area index (LAI) and above-ground biomass (AGB) estimation at big trumpet and milk stages using the linear regression-based feature augmentation (LRFA) and conventional (CONV) methods. (The best estimation for each phenotype is highlighted in boldface).

Growth stage	Data type	Metric	LAI		AGB (kg/ha)	
			CONV	LRFA	-	CONV
Big trumpet	MS	R^2	0.726	/		0.625
		RMSE	0.276	/		94.4
	RGB	R^2	0.703	/		0.622
		RMSE	0.284	/		95.2
	TIR	R^2	0.609	/		0.618
		RMSE	0.331	/		97.3
	3D	R^2	0.717	/		0.570
		RMSE	0.272	/		101.3
	MS + RGB + TIR	R^2	0.738	0.717		0.667
		RMSE	0.270	0.273		90.1
Milk	MS + RGB + 3D	R^2	0.766	0.791		0.651
		RMSE	0.252	0.235		91.0
	RGB + TIR + 3D	R^2	0.753	0.776		0.674
		RMSE	0.257	0.242		89.9
	MS + TIR + 3D	R^2	0.762	0.766		0.666
		RMSE	0.256	0.250		90.3
	MS + RGB + TIR + 3D	R^2	0.747	0.768		0.668
		RMSE	0.267	0.246		89.6

outperformed the other two types of data for estimating AGB, with R^2 values of 0.365 and 0.416, respectively. Thermal data ranked third with R^2 value of 0.238, while 3D data performed the worst with R^2 value of 0.117. Multi-source data fusion generally produced more accurate estimations compared to single-source data. When fusing MS, TIR, and 3D features using the LRFA method, the highest prediction accuracy was achieved, with an R^2 value of 0.480 and an RMSE of 347.9 kg/ha.

3.2.3. Comparison of the conventional method with LRFA

According to Table 1, in most scenarios involving the integration of data from multiple sources, the LRFA method yielded more accurate phenotype estimations compared to the conventional approach. In addition, the comprehensive comparison of cross-validation accuracy between the LRFA method and the conventional one when combining multi-source data is presented in Fig. 7. Each box plot represents the results of 100 validations conducted by the random forest during a 5-fold cross-validation process for LAI and AGB estimation at both stages. Out of these 100 cross-validation runs, the LRFA method outperformed the conventional method in 67 instances. The mean R^2 value for the LRFA method was 0.619, surpassing the conventional method's 0.589, underscoring the effectiveness of the proposed feature augmentation technique.

The number of cycles in LRFA method determines the number of newly generated features. To investigate the number of cycles in LRFA on the fusion effect, the performances of the random forest model for

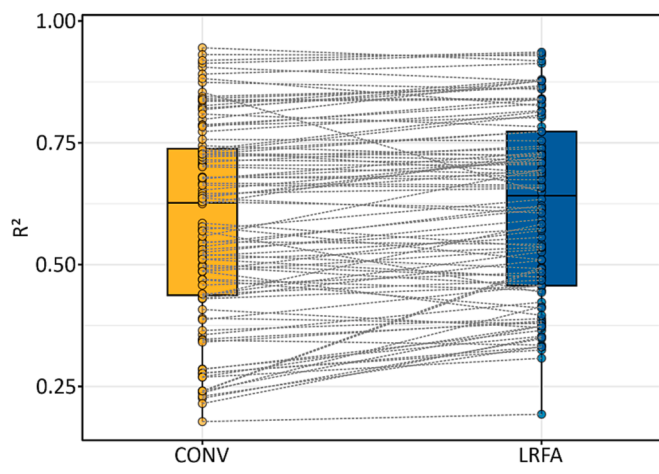


Fig. 7. Comprehensive comparison of modeling accuracy between linear regression-based feature augmentation (LRFA) and conventional (CONV) methods. Box and dot points show the distribution of R^2 for 5-fold cross-validation in 5 combinations of multi-source data in the LAI and AGB estimations during the big trumpet and milk stages. Each box plot consists of 100 samples ($4 \times 5 \times 5$).

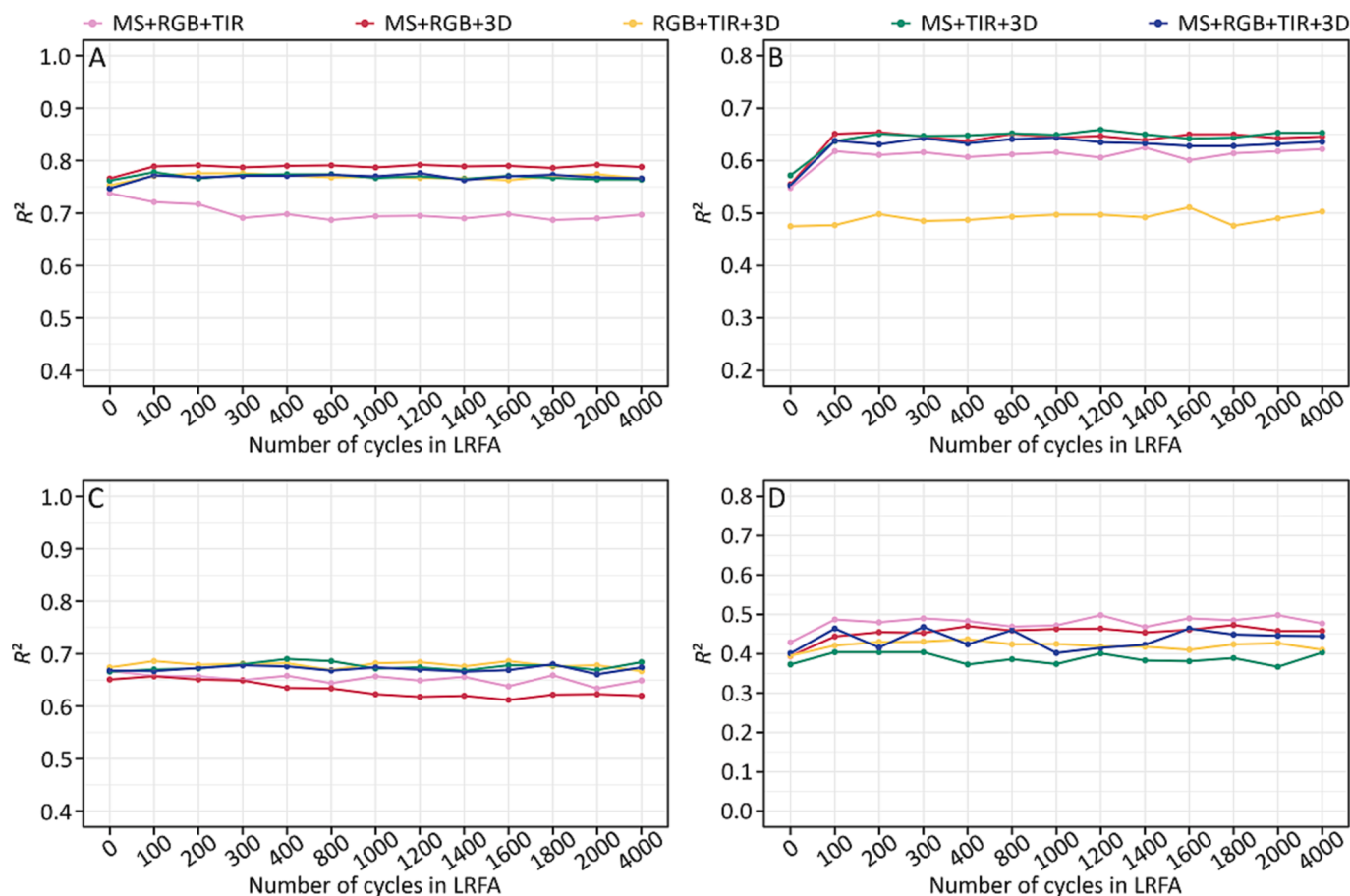


Fig. 8. The relationship between the number of cycles and random forest model accuracy in linear regression-based feature augmentation method. A and B are the estimation accuracy of leaf area index at the big trumpet and milk stages, respectively. C and D are the estimation accuracy of above-ground biomass at the big trumpet and milk stages, respectively.

different cycle numbers were explored. As shown in Fig. 8, the results demonstrate that the model performance remains stable and increasing the number of cycles does not improve the random forest model. The model performed ideally for a cycle number of 100 and also performed better than the conventional fusion method in most cases.

3.3. Analysis of phenotypic trait estimates

Measured and estimated LAI and AGB for both the two growth stages using the best-performing model are shown in Fig. 9. Visually, the maps of the estimated phenotypes showed good agreement with the measured phenotypes. The *t*-test was implemented to evaluate the differences between the estimated and measured phenotypes within each genotype and treatment. There was no significant difference ($P > 0.05$) between the estimated and measured plant phenotypes for each nitrogen treatment in both stages (Fig. 10). Similarly, no significant difference ($P > 0.05$) was found between the estimated and measured plant phenotypes for each genotype (Fig. 10). The performance of each best-performing model to detect phenotypic differences across genotypes and nitrogen treatments was evaluated using combined ANOVA (Table 2). The measured AGB at milk stage was able to detect significant differences across genotypes and treatments. In the rest of cases, the measured phenotypic values were only able to detect differences across treatments. The estimated phenotypes had the same properties as measured phenotypes in detecting differences across genotypes and nitrogen treatments.

4. Discussion

4.1. Advantages of CCO photography technology

Low-cost RGB nadir photography is capable of generating point cloud data to extract structural information, but the quality of the generated point clouds is often poor. This is due to its lack of involvement of plant side photographs in the 3D point cloud model construction process, which is crucial for establishing the target side detail texture and generating point clouds (Chen et al., 2022; Jurado et al., 2020). Oblique photography is a new technique for 3D modeling of urban areas and forestry, achieved by tilting the UAV-mounted RGB camera at a specific angle from the vertical to capture oblique images (Che et al., 2020). Compared to nadir photography (Hassan et al., 2019a), oblique photography provides more detailed information about the object's sides and bottom, resulting in a denser point cloud and more effective 3D reconstruction. Although conventional oblique photography is a common method for extracting plant structural parameters, the results are not always satisfactory due to the lack of more angular plant images. For instance, when assessing the height of faba bean plants (Ji et al., 2022), it has been found to be less accurate than nadir photography. Oblique photography has also been used to assess maize plant height, with only 1.1 % improvement in accuracy compared to nadir photography (Che et al., 2020). The surround photography is well-suited for creating precise object models, but its practical use is often restricted to smaller-scale applications with ground-based cameras (Xiao et al., 2020), making it challenging to apply in field settings. The emerging technology of UAV CCO photography has overcome this limitation. In this

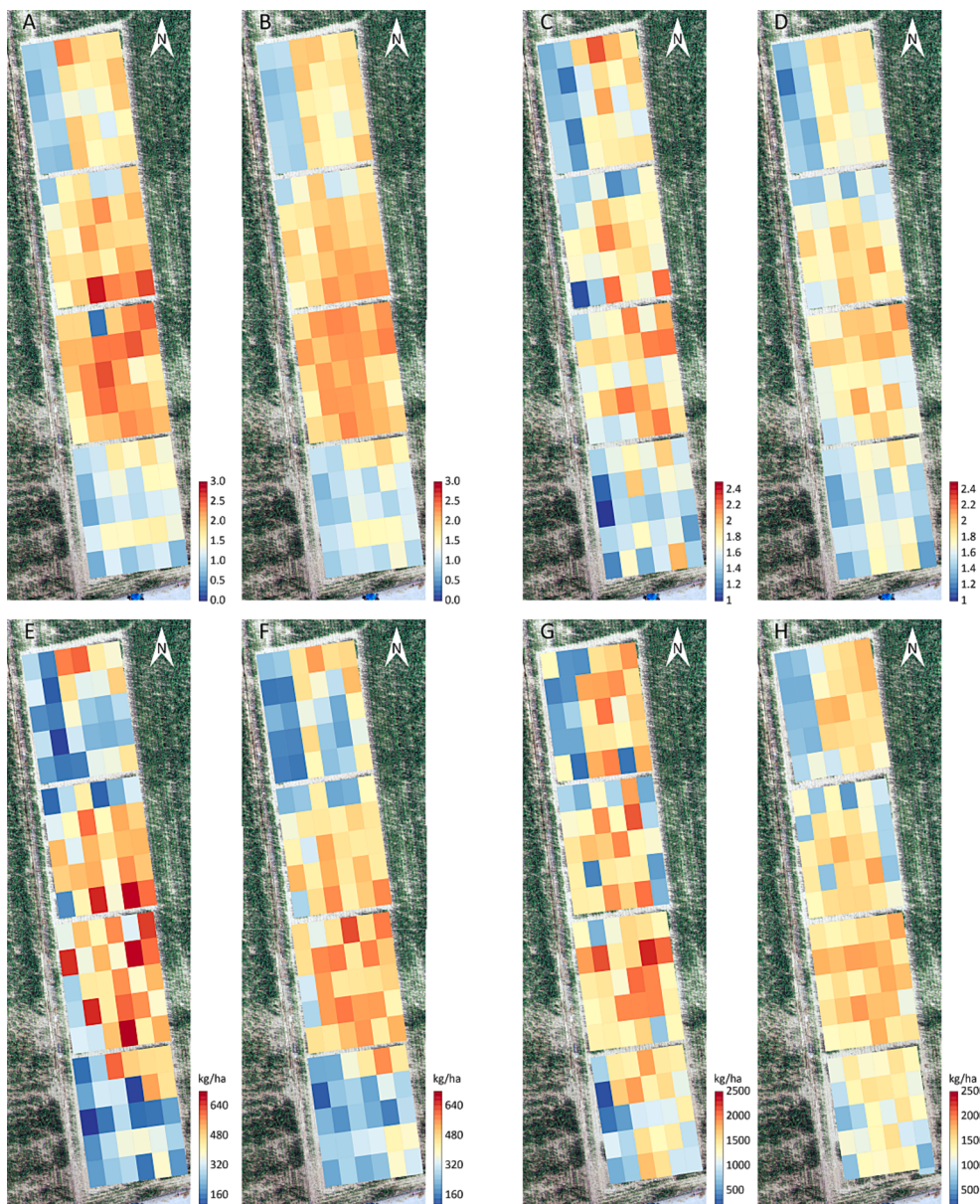


Fig. 9. Spatial distribution of measured phenotypes and estimated plant phenotypes from the best performing models. A and B represent the measured and the estimated leaf area index at the big trumpet stage, respectively. C and D represent the measured and the estimated leaf area index at the milk stage, respectively. E and F represent the measured and the estimated above-ground biomass at the big trumpet stage. G and H represent the measured and the estimated above-ground biomass at the milk stage.

study, CCO photography with the use of two drones yielded a net flight time of approximately one hour. Based on our previous research (Xiao et al., 2023), as image quality increases, the time required for CCO photography can be significantly reduced. In the future, it is worth exploring the use of higher pixel cameras to execute CCO photography tasks more efficiently.

In recent study (Xiao et al., 2023), we compared the 3D reconstruction accuracy of CCO photography with the most commonly used oblique photography method for UAV, i.e., five-directional oblique (FDO) photography. The CCO photography-derived 3D canopy models provided higher accuracy than the FDO photography-derived 3D canopy models in the estimation of organ-scale traits, further demonstrating the effectiveness of the CCO approach in capturing crop traits. The CCO photography also has two other advantages over the FDO photography: (1) CCO is more efficient than FDO routes, with CCO photography

requiring far fewer images at different altitudes than FDO photography, averaging only 38 % of FDO photography (Xiao et al., 2023). (2) CCO photography can image at ultra-low altitude without disturbing the canopy structure, whereas the conventional oblique method may disturb the canopy at this altitude. This is because the shooting area of CCO photography is located at the center of the circular route, away from the interference zone at the edge of the flight path. In contrast, conventional oblique photography methods face challenges when using the same ultra-low altitude method. If downdrafts from the rotor blades of the drone disturbed the canopy at the previous waypoint, problems could arise at the next waypoint (Xiao et al., 2023). Disturbances introduced in one area of the canopy can propagate to the next, affecting data quality and potentially compromising the accuracy of the assessment.

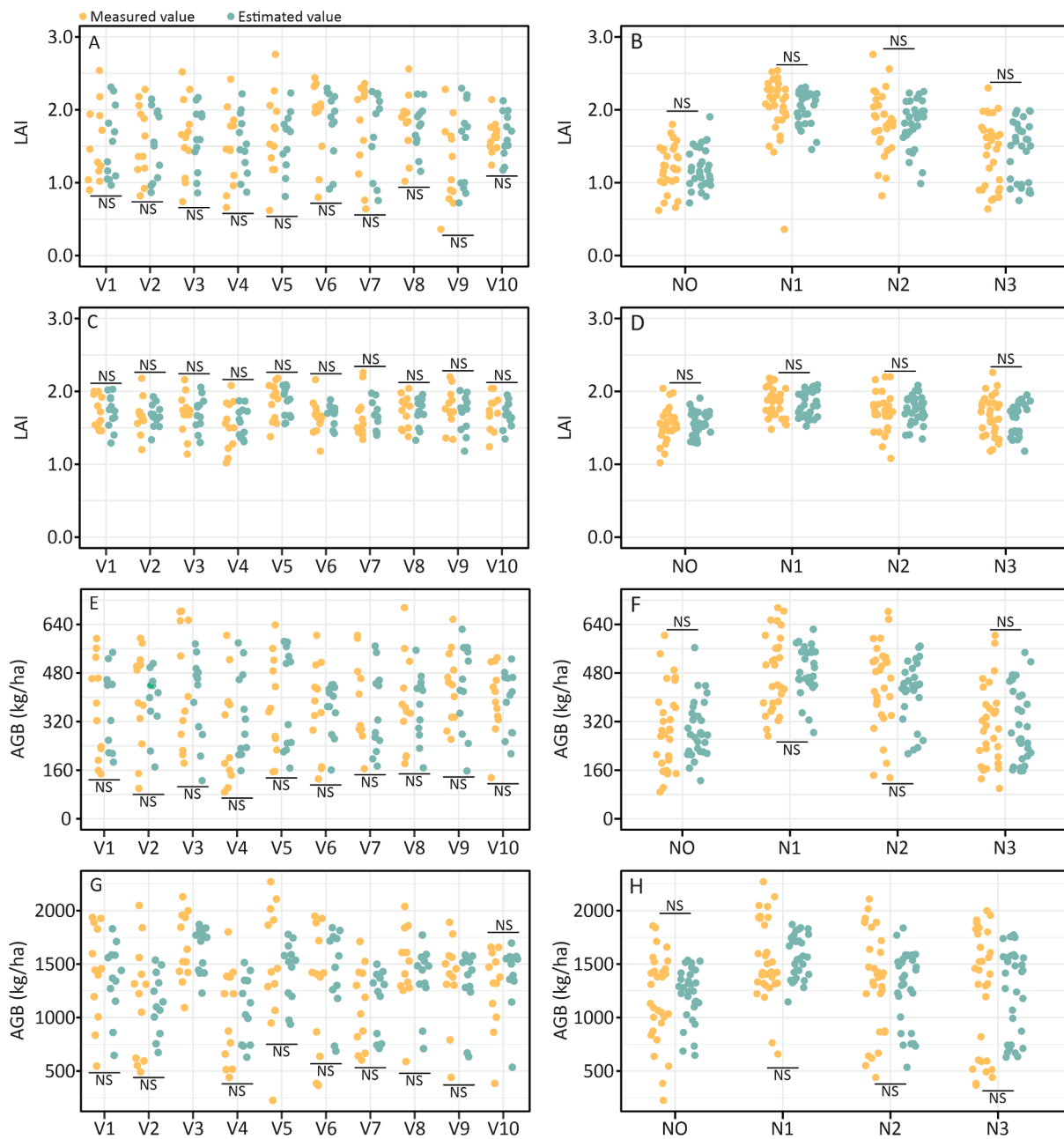


Fig. 10. Distribution of measured and estimated phenotype value for each genotype and treatment. A and B are the distribution of measured and estimated leaf area index values at the big trumpet stage within each variety and each treatment, respectively. C and D are the distribution of measured and estimated leaf area index values at the milk stage within each variety and each treatment, respectively. E and F are the distribution of measured and estimated above-ground biomass values at the big trumpet stage within each variety and each treatment, respectively. G and H are the distribution of measured and estimated above-ground biomass values at the milk stage within each variety and each treatment, respectively. NS, no significant ($P > 0.05$). V1-V10 are the codes of different varieties (Table S1). NO-N3 represent the different nitrogen treatments.

4.2. Multi-source data fusion for estimating plant phenotypes

In the field of plant phenotyping, it is common to fuse data from RGB, MS, and TIR sensors. The characteristics of these three types of sensor data were described in numerous studies (Fei et al., 2023b; Maimaitijiang et al., 2020) and will not be discussed further in this section. The use of dense point cloud data (e.g., from LiDAR) in plant phenotyping is a relatively new approach that has the potential to provide valuable information on plant structure and architecture. For example, Chen et al. (2022) predicted individual apple tree yield by combining morphological features extracted from LiDAR data and MS information. The crown volume 1 derived from the LiDAR point cloud data contributed the most

for the prediction model. In addition, when LiDAR-extracted data were combined with thermal data as predictors for Bayesian ridge regression and support vector regression algorithms, higher prediction accuracy was achieved compared to the combination of thermal, RGB, and MS data (Wang et al., 2022). The combination of nadir photography derived MS, RGB, and TIR data achieved the best accuracy for estimating maize LAI in previous report (Liu et al., 2021b). The same situations occurred in the phenotypic evaluation of other crops (Fei et al., 2023b; Maimaitijiang et al., 2020). However, results in this study showed that the highest maize LAI estimation accuracy was achieved using the combination of MS, RGB, and 3D features at both measured stages. Similarly, the most accurate AGB estimates can be obtained using a data

Table 2

Analysis of variance for measured and estimated phenotypic values.

Growth stage	Trait	F-value	
		Genotype	Treatment
Big trumpet	Measured LAI	1.63	33.16***
	Estimated LAI	1.09	53.58***
	Measured AGB	1.87	23.66***
	Estimated AGB	1.09	33.28***
Milk	Measured LAI	1.71	9.07***
	Estimated LAI	2.15	15.97***
	Measured AGB	2.78**	4.22**
	Estimated AGB	6.91**	16.53**

LAI leaf area index, AGB above-ground biomass.

combination (RGB + TIR + 3D) including 3D features in the big trumpet stage. These findings illustrate the limitations of nadir photography data to estimate plant traits and highlight the advantages of accurate morphological features extracted from 3D canopy model. Model performance is usually not optimal when data from all four sources are merged simultaneously. This may be attributed to the problem of redundancy of information due to the fusion of data from multiple sources (Pohl and Van Genderen, 1998), which has also been observed in Maimaitijiang et al. (2017). Therefore, the optimal combination of multi-source data for estimating crop phenotypes still needs to be further researched and explored in the future.

4.3. Characteristics of LRFA method

The conventional data fusion method for plant phenotyping is to combine data from different sources (e.g., MS, RGB, TIR, and 3D data) into a single dataset for predictive modeling of target plant traits. In other industries, there were many other data fusion methods such as simple averaging, BatesGranger averaging (Bates and Granger, 1969), Granger-Ramanathan averaging (Granger and Ramanathan, 1984), Bayesian model averaging (Xu et al., 2019) and bias-corrected eigenvector averaging (Hsiao and Wan, 2014). This diversity of approaches shows that researchers are always looking for innovative ways to improve the accuracy and efficiency of data fusion models. The LRFA proposed in this study aims to derive numerous new high-quality features that contain information from multiple sources of data. The idea of using cross-validation to generate new training features is drawn from the method used to generate the second level training set in stacking regression (Fei et al., 2021). Overall, the accuracy of the LRFA based data fusion method was higher than that of conventional method (Fig. 7). When employing the LRFA technique, the newly generated features, obtained by combining information from multiple sources through training, exhibit a higher correlation with phenotypes (Fig.S2). Through iterations, the hundreds of randomly generated and precise features produced by LRFA can enhance the signal-to-noise ratio of the overall features, thereby increasing the final accuracy of the model. In principle, the LFRA approach may render noise-sensitive regression algorithms more effective. In the future, the LRFA approach should be tested in data fusion applications of different domains, which can provide valuable insights into its potential strengths and limitations, and identify areas for further research and development.

4.4. Effect of developmental stage on the accuracy of phenotype estimation

The accuracy of phenotype estimation at the big trumpet stage is higher than that at the milk stage, likely due to the following reasons. Firstly, at the big trumpet stage, the coefficients of variation for canopy height, LAI, and AGB were 25.9 %, 32.0 %, and 40.5 %, respectively. In comparison, at the milk stage, the coefficients of variation for each phenotype were 9.4 %, 15.6 %, and 35.7 %, respectively. The big

trumpet stage exhibited greater phenotypic variability, resulting in increased data variability and improved predictive capabilities of the model (Ferrio et al., 2005). The big trumpet stage in maize, occurring about 45 days after sowing, represents a critical phase of growth and reproduction. In our study of ten different maize varieties, genetic differences in growth rate, plant size, disease resistance, and adaptability to climate result in significant variation in appearance at this stage. As time passes, maize varieties tend to reach similar growth states, reducing phenotypic differences. During later growth stages (milk stage), competition for limited resources like nutrients, water, and sunlight further narrows the differences among varieties. Additionally, common factors such as nutrient depletion, diseases, and pests have similar effects on all varieties, reducing variability. Secondly, during the milk stage, maize tassels become more visible in UAV images, obstructing the lower leaves and potentially leading to a loss of leaf information, which may reduce the accuracy of estimation models based on UAV images following maize tasseling (Liu et al., 2021b).

Although AGB is a trait with 3D properties, the accuracy of AGB estimation using 3D features was much lower during the milk stage compared to that of MS and RGB features, possibly due to the influence of ears. Ears exhibit higher dry matter partitioning during the late growth stage of maize, and a study by Cai et al. (2022) found that ears can account for up to 44 % of AGB during the milk stage. However, it is difficult to assess the quality of ears using volumetric information obtained by CCO photography. This limitation may contribute to lower accuracy in the assessment of AGB using 3D features at the milk stage. As a result, CCO photography is more suitable for AGB estimation in the early growth stage of maize.

5. Summary and conclusions

The utilization of UAV-based imaging for plant phenotyping is gaining increasing popularity due to its capacity to non-invasively capture high-resolution data over extensive areas. In this investigation, a novel strategy, LRFA, was introduced to augment features from UAV nadir and CCO photography for the estimation of maize phenotypes. The key findings can be summarized as follows:

- (a) CCO photography technology exhibited superior accuracy in extracting canopy height compared to nadir photography at both growth stages.
- (b) The incorporation of CCO photography-derived data improved LAI and AGB estimations at the big trumpet stage and LAI estimation at the milk stage when contrasted with the combination of multi-sensor nadir photography data.
- (c) In most instances, the LRFA method outperformed the conventional method for LAI and AGB estimation.

The results offered in this study underscore that combining different photography techniques and applying the feature augmentation method can enhance the accuracy of phenotype estimation, thereby advancing our comprehension of plant growth and development. To assess the robustness of this approach, it is advisable to subject it to testing across various crop types, a broader range of genotypes, and under varying growth stages and environmental conditions.

CRediT authorship contribution statement

Shuaipeng Fei: Data curation, Investigation, Software, Writing – original draft. **Shunfu Xiao:** Data curation, Methodology. **Qing Li:** Data curation, Software. **Meiyang Shu:** Data curation. **Weiguang Zhai:** Data curation. **Yonggui Xiao:** Writing – review & editing. **Zhen Chen:** Conceptualization, Methodology, Writing – review & editing. **Helong Yu:** Writing – review & editing. **Yuntao Ma:** Supervision, Writing – review & editing.

Declaration of Competing Interest

The authors declare that they have no known competing financial interests or personal relationships that could have appeared to influence the work reported in this paper.

Data availability

Data will be made available on request.

Acknowledgments

This research was funded by the Key Technologies Research and Development Program of China (2022YFD1900801), the Beijing Digital Agriculture Innovation Consortium Project (BAIC10-2023), the National Natural Science Foundation of China (32271987), the Inner Mongolia Science and technology project (NO. 2022ZY0128-01).

Appendix A. Supplementary material

Supplementary data to this article can be found online at <https://doi.org/10.1016/j.compag.2023.108462>.

References

- Aasen, H., Burkart, A., Bolten, A., Bareth, G., 2015. Generating 3D hyperspectral information with lightweight UAV snapshot cameras for vegetation monitoring: from camera calibration to quality assurance. *ISPRS J. Photogramm. Remote Sens.* 108, 245–259. <https://doi.org/10.1016/j.isprsjprs.2015.08.002>.
- Awika, H.O., Bedre, R., Yeom, J., Marconi, T.G., Enciso, J., Mandadi, K.K., Jung, J., Avila, C.A., 2019. Developing growth-associated molecular markers via high-throughput phenotyping in Spinach. *Plant Genome* 12, 190027. <https://doi.org/10.3835/plantgenome2019.03.0027>.
- Bates, J.M., Granger, C.W.J., 1969. The combination of forecasts. *J. Oper. Res. Soc.* 20, 451–468. <https://doi.org/10.1057/jors.1969.103>.
- Bendig, J., Yu, K., Aasen, H., Bolten, A., Bennertz, S., Broscheit, J., Gnyp, M.L., Bareth, G., 2015. Combining UAV-based plant height from crop surface models, visible, and near infrared vegetation indices for biomass monitoring in barley. *Int. J. Appl. Earth Obs. Geoinformation* 39, 79–87. <https://doi.org/10.1016/j.jag.2015.02.012>.
- Breiman, L., 2001. Random forests. *Mach. Learn.* 45, 5–32. <https://doi.org/10.1023/a:1010933404324>.
- Cai, F., Zhang, Y., Mi, N., Ming, H., Zhang, S., Zhang, H., Zhao, X., Zhang, B., 2022. The effect of drought and sowing date on dry matter accumulation and partitioning in the above-ground organs of maize. *Atmos.* 13, 677. <https://doi.org/10.3390/atmos13050677>.
- Chang, A., Jung, J., Yeom, J., Landivar, J., 2021. 3D characterization of sorghum panicles using a 3D point cloud derived from UAV imagery. *REMOTE Sens.* 13 <https://doi.org/10.3390/rs13020282>.
- Che, Y., Wang, Q., Xie, Z., Zhou, L., Li, S., Hui, F., Wang, X., Li, B., Ma, Y., 2020. Estimation of maize plant height and leaf area index dynamics using an unmanned aerial vehicle with oblique and nadir photography. *Ann. Bot.* 126, 765–773. <https://doi.org/10.1093/aob/mcaa097>.
- Chen, R., Zhang, C., Xu, B., Zhu, Y., Zhao, F., Han, S., Yang, G., Yang, H., 2022. Predicting individual apple tree yield using UAV multi-source remote sensing data and ensemble learning. *Comput. Electron. Agric.* 201, 107275 <https://doi.org/10.1016/j.compag.2022.107275>.
- Chianucci, F., Disperati, L., Guzzi, D., Bianchini, D., Nardino, V., Lastri, C., Rindinella, A., Corona, P., 2016. Estimation of canopy attributes in beech forests using true colour digital images from a small fixed-wing UAV. *Int. J. Appl. Earth Obs. Geoinformation* 47, 60–68. <https://doi.org/10.1016/j.jag.2015.12.005>.
- Ding, F., Li, C., Zhai, W., Fei, S., Cheng, Q., Chen, Z., 2022. Estimation of nitrogen content in winter wheat based on multi-source data fusion and machine learning. *Agriculture* 12, 1752. <https://doi.org/10.3390/agriculture12111752>.
- Fei, S., Hassan, M.A., He, Z., Chen, Z., Shu, M., Wang, J., Li, C., Xiao, Y., 2021. Assessment of ensemble learning to predict wheat grain yield based on UAV multispectral reflectance. *Remote Sens.* 13, 2338. <https://doi.org/10.3390/rs13122338>.
- Fei, S., Chen, Z., Li, L., Ma, Y., Xiao, Y., 2023a. Bayesian model averaging to improve the yield prediction in wheat breeding trials. *Agric. For. Meteorol.* 328, 109237 <https://doi.org/10.1016/j.agrformet.2022.109237>.
- Fei, S., Hassan, M.A., Xiao, Y., Su, X., Chen, Z., Cheng, Q., Duan, F., Chen, R., Ma, Y., 2023b. UAV-based multi-sensor data fusion and machine learning algorithm for yield prediction in wheat. *Precis. Agric.* 24, 187–212. <https://doi.org/10.1007/s11119-022-09938-8>.
- Feng, A., Zhou, J., Vories, E.D., Sudduth, K.A., Zhang, M., 2020. Yield estimation in cotton using UAV-based multi-sensor imagery. *Biosyst. Eng.* 193, 101–114. <https://doi.org/10.1016/j.biosystemseng.2020.02.014>.
- Ferrio, J.P., Villegas, D., Zarco, J., Aparicio, N., Araus, J.L., Royo, C., 2005. Assessment of durum wheat yield using visible and near-infrared reflectance spectra of canopies. *Field Crops Res.* 94, 126–148. <https://doi.org/10.1016/j.fcr.2004.12.002>.
- Floreano, D., Wood, R.J., 2015. Science, technology and the future of small autonomous drones. *Nature* 521, 460–466. <https://doi.org/10.1038/nature14542>.
- Garza, B., Ancona, V., Enciso, J., Perotto-Baldvieso, H., Kunta, M., Simpson, C., 2020. Quantifying citrus tree health using true color UAV images. *REMOTE Sens.* 12, <https://doi.org/10.3390/rs12010170>.
- Granger, C.W.J., Ramanathan, R., 1984. Improved methods of combining forecasts. *J. Forecast.* 3, 197–204. <https://doi.org/10.1002/for.3980030207>.
- Han, L., Yang, G., Yang, H., Xu, B., Li, Z., Yang, X., 2018. Clustering field-based maize phenotyping of plant-height growth and canopy spectral dynamics using a UAV remote-sensing approach. *Front. Plant Sci.* 9, 1638. <https://doi.org/10.3389/fpls.2018.01638>.
- Han, L., Yang, G., Dai, H., Xu, B., Yang, H., Feng, H., Li, Z., Yang, X., 2019. Modeling maize above-ground biomass based on machine learning approaches using UAV remote-sensing data. *Plant Methods* 15, 10. <https://doi.org/10.1186/s13007-019-0394-z>.
- Haralick, R.M., Shanmugam, K., Dinstein, I., 1973. Textural features for image classification. *IEEE Trans. Syst. Man Cybern. SMC-3*, 610–621. <https://doi.org/10.1109/TSMC1973.4309314>.
- Hassan, M.A., Yang, M., Fu, L., Rasheed, A., Zheng, B., Xia, X., Xiao, Y., He, Z., 2019a. Accuracy assessment of plant height using an unmanned aerial vehicle for quantitative genomic analysis in bread wheat. *Plant Methods* 15, 37. <https://doi.org/10.1186/s13007-019-0419-7>.
- Hassan, M.A., Yang, M., Rasheed, A., Yang, G., Reynolds, M., Xia, X., Xiao, Y., He, Z., 2019b. A rapid monitoring of NDVI across the wheat growth cycle for grain yield prediction using a multi-spectral UAV platform. *Plant Sci.* 282, 95–103. <https://doi.org/10.1016/j.plantsci.2018.10.022>.
- Hou, M., Tian, F., Ortega-Farias, S., Riveros-Burgos, C., Zhang, T., Lin, A., 2021. Estimation of crop transpiration and its scale effect based on ground and UAV thermal infrared remote sensing images. *Eur. J. Agron.* 131, 126389 <https://doi.org/10.1016/j.eja.2021.126389>.
- Hsiao, C., Wan, S.K., 2014. Is there an optimal forecast combination? *Recent Adv. Time Ser. Econom.* 178, 294–309. <https://doi.org/10.1016/j.jeconom.2013.11.003>.
- Ji, Y., Chen, Z., Cheng, Q., Liu, R., Li, M., Yan, X., Li, G., Wang, D., Fu, L., Ma, Y., Jin, X., Zong, X., Yang, T., 2022. Estimation of plant height and yield based on UAV imagery in faba bean (*Vicia faba* L.). *Plant Methods* 18, 26. <https://doi.org/10.1186/s13007-022-00861-7>.
- Jiang, J., Johansen, K., Stanschewski, C.S., Wellman, G., Mousa, M.A.A., Fiene, G.M., Asiry, K.A., Tester, M., McCabe, M.F., 2022. Phenotyping a diversity panel of quinoa using UAV-derived leaf area index, SPAD-based chlorophyll and a random forest approach. *Precis. Agric.* 23, 961–983. <https://doi.org/10.1007/s11119-021-09870-3>.
- Jurado, J.M., Ortega, L., Cubillas, J.J., Feito, F.R., 2020. Multispectral mapping on 3D models and multi-temporal monitoring for individual characterization of olive trees. *Remote Sens.* 12, 1106. <https://doi.org/10.3390/rs12071106>.
- Kendig, K., 2000. Is a 2000-year-old formula still keeping some secrets? *Am. Math. Mon.* 107, 402–415. <https://doi.org/10.2307/2695295>.
- Li, B., Xu, X., Zhang, L., Han, J., Bian, C., Li, G., Liu, J., Jin, L., 2020. Above-ground biomass estimation and yield prediction in potato by using UAV-based RGB and hyperspectral imaging. *ISPRS J. Photogramm. Remote Sens.* 162, 161–172. <https://doi.org/10.1016/j.isprsjprs.2020.02.013>.
- Liu, S., Jin, X., Nie, C., Wang, S., Yu, X., Cheng, M., Shao, M., Wang, Z., Tuohuti, N., Bai, Y., Liu, Y., 2021b. Estimating leaf area index using unmanned aerial vehicle data: shallow vs. deep machine learning algorithms. *Plant Physiol.* 187, 1551–1576. <https://doi.org/10.1093/plphys/kiab322>.
- Liu, F., Song, Q., Zhao, J., Mao, L., Bu, H., Hu, Y., Zhu, X., 2021a. Canopy occupation volume as an indicator of canopy photosynthetic capacity. *New Phytol.* 232, 941–956. <https://doi.org/10.1111/nph.17611>.
- Maimaitijiang, M., Ghulam, A., Sidike, P., Hartling, S., Maimaitiyiming, M., Peterson, K., Shavers, E., Fishman, J., Peterson, J., Kadam, S., Burken, J., Fritsch, F., 2017. Unmanned Aerial System (UAS)-based phenotyping of soybean using multi-sensor data fusion and extreme learning machine. *ISPRS J. Photogramm. Remote Sens.* 134, 43–58. <https://doi.org/10.1016/j.isprsjprs.2017.10.011>.
- Maimaitijiang, M., Sagan, V., Sidike, P., Hartling, S., Esposito, F., Fritsch, F.B., 2020. Soybean yield prediction from UAV using multimodal data fusion and deep learning. *Remote Sens. Environ.* 237, 111599. <https://doi.org/10.1016/j.rse.2019.111599>.
- Montesinos-López, O.A., Martín-Vallejo, J., Crossa, J., Gianola, D., Hernández-Suárez, C. M., Montesinos-López, A., Juliana, P., Singh, R., 2019. A benchmarking between deep learning, support vector machine and Bayesian threshold best linear unbiased prediction for predicting ordinal traits in plant breeding. *G3 Genes Genomes Genetics* 9, 601–618. <https://doi.org/10.1534/g3.118.200998>.
- Pan, L., Xia, H., Yang, J., Niu, W., Wang, R., Song, H., Guo, Y., Qin, Y., 2021. Mapping cropping intensity in Huaibei basin using phenology algorithm, all Sentinel-2 and Landsat images in Google Earth Engine. *Int. J. Appl. Earth Obs. Geoinformation* 102, 102376. <https://doi.org/10.1016/j.jag.2021.102376>.
- Pipatsitee, P., Tisarum, R., Taota, K., Samphumphuang, T., Eiumnoh, A., Singh, H.P., Cha-um, S., 2023. Effectiveness of vegetation indices and UAV-multiplespectral imagers in assessing the response of hybrid maize (*Zea mays* L.) to water deficit stress under field environment. *Environ. Monit. Assess.* 195, 128. <https://doi.org/10.1007/s10661-022-10766-6>.
- Pohl, C., Van Genderen, J.L., 1998. Review article Multisensor image fusion in remote sensing: Concepts, methods and applications. *Int. J. Remote Sens.* 19, 823–854. <https://doi.org/10.1080/014311698215748>.

- Qin, W., Wang, J., Ma, L., Wang, F., Hu, N., Yang, X., Xiao, Y., Zhang, Y., Sun, Z., Wang, Z., Yu, K., 2022. UAV-based multi-temporal thermal imaging to evaluate wheat drought resistance in different deficit irrigation regimes. *Remote Sens.* 14, 5608. <https://doi.org/10.3390/rs14215608>.
- Shao, G., Han, W., Zhang, H., Zhang, L., Wang, Y., Zhang, Y., 2023. Prediction of maize crop coefficient from UAV multisensor remote sensing using machine learning methods. *Agric Water Manag* 276, 108064. <https://doi.org/10.1016/j.agwat.2022.108064>.
- Shu, M., Fei, S., Zhang, B., Yang, X., Guo, Y., Li, B., Ma, Y., 2022a. Application of UAV Multisensor Data and Ensemble Approach for High-Throughput Estimation of Maize Phenotyping Traits. *Plant Phenomics* 2022, 9802585. 10.34133/2022/9802585.
- Shu, M., Shen, M., Dong, Q., Yang, X., Li, B., Ma, Y., 2022b. Estimating the maize above-ground biomass by constructing the tridimensional concept model based on UAV-based digital and multi-spectral images. *Field Crops Res.* 282, 108491 <https://doi.org/10.1016/j.fcr.2022.108491>.
- Sidike, P., Sagan, V., Qumsiyeh, M., Maimaitijiang, M., Essa, A., Asari, V., 2018. Adaptive trigonometric transformation function with image contrast and color enhancement: application to unmanned aerial system imagery. *IEEE Geosci. Remote Sens. Lett.* 15, 404–408. <https://doi.org/10.1109/LGRS.2018.2790899>.
- Tester, M., Langridge, P., 2010. Breeding technologies to increase crop production in a changing World. *Science* 327, 818–822. <https://doi.org/10.1126/science.1183700>.
- Wallace, L., 2013. Assessing the stability of canopy maps produced from UAV-LiDAR data. 2013. *IEEE Int. Geosci. Remote Sens. Symp. Igars* 3879–3882. <https://doi.org/10.1109/IGARSS.2013.6723679>.
- Wan, L., Zhang, J., Dong, X., Du, X., Zhu, J., Sun, D., Liu, Y., He, Y., Cen, H., 2021. Unmanned aerial vehicle-based field phenotyping of crop biomass using growth traits retrieved from PROSAIL model. *Comput. Electron. Agric.* 187, 106304 <https://doi.org/10.1016/j.compag.2021.106304>.
- Wang, Q., Che, Y., Shao, K., Zhu, J., Wang, R., Sui, Y., Guo, Y., Li, B., Meng, L., Ma, Y., 2022. Estimation of sugar content in sugar beet root based on UAV multi-sensor data. *Comput. Electron. Agric.* 203, 107433 <https://doi.org/10.1016/j.compag.2022.107433>.
- Wu, J., Wen, S., Lan, Y., Yin, X., Zhang, J., Ge, Y., 2022. Estimation of cotton canopy parameters based on unmanned aerial vehicle (UAV) oblique photography. *Plant Methods* 18, 129. <https://doi.org/10.1186/s13007-022-00966-z>.
- Xiao, Q., Bai, X., Zhang, C., He, Y., 2022. Advanced high-throughput plant phenotyping techniques for genome-wide association studies: A review. *J. Adv. Res.* 35, 215–230. <https://doi.org/10.1016/j.jare.2021.05.002>.
- Xiao, S., Chai, H., Shao, K., Shen, M., Wang, Q., Wang, R., Sui, Y., Ma, Y., 2020. Image-based dynamic quantification of aboveground structure of sugar beet in field. *Remote Sens.* 12, 269. <https://doi.org/10.3390/rs12020269>.
- Xiao, S., Ye, Y., Fei, S., Chen, H., Cai, Z., Che, Y., Wang, Q., Ghafoor, A., Bi, K., Shao, K., 2023. High-throughput calculation of organ-scale traits with reconstructed accurate 3D canopy structures using a UAV RGB camera with an advanced cross-circling oblique route. *ISPRS J. Photogramm. Remote Sens.* 201, 104–122. <https://doi.org/10.1016/j.isprsjprs.2023.05.016>.
- Xie, C., Yang, C., 2020. A review on plant high-throughput phenotyping traits using UAV-based sensors. *Comput. Electron. Agric.* 178, 105731 <https://doi.org/10.1016/j.compag.2020.105731>.
- Xu, D., Zhao, R., Li, S., Chen, S., Jiang, Q., Zhou, L., Shi, Z., 2019. Multi-sensor fusion for the determination of several soil properties in the Yangtze River Delta, China: Predictions based on multi-sensor fusion. *Eur. J. Soil Sci.* 70, 162–173. <https://doi.org/10.1111/ejss.12729>.
- Yue, J., Feng, H., Jin, X., Yuan, H., Li, Z., Zhou, C., Yang, G., Tian, Q., 2018. A Comparison of Crop Parameters Estimation Using Images from UAV-Mounted Snapshot Hyperspectral Sensor and High-Definition Digital Camera. *Remote Sens.* 10, 1138. <https://doi.org/10.3390/rs10071138>.
- Yue, J., Yang, H., Yang, G., Fu, Y., Wang, H., Zhou, C., 2023. Estimating vertically growing crop above-ground biomass based on UAV remote sensing. *Comput. Electron. Agric.* 205, 107627 <https://doi.org/10.1016/j.compag.2023.107627>.